Title

Dynamics of primary and secondary microbubbles created by laser-induced breakdown of an optically trapped nanoparticle

Journal

Physical Review E, 85(1)

ISSN

2470-0045

Authors

Arita, Y

Antkowiak, M

Venugopalan, V

et al.

Publication Date

2012

DOI

10.1103/physreve.85.016319

Dynamics of primary and secondary microbubbles created by laser-induced breakdown of an optically trapped nanoparticle

Y. Arita,[1,*] M. Antkowiak,[1,2,*] V. Venugopalan,[3,4] F. J. Gunn-Moore,[2] and K. Dholakia[1]

[1]*SUPA, School of Physics and Astronomy, University of St Andrews, St Andrews, Fife, KY16 9SS, United Kingdom*

[2]*SULSA, School of Biology, Medical and Biological Sciences Building, North Haugh, University of St Andrews, St Andrews, Fife, KY16 9TF, United Kingdom*

[3]*Department of Chemical Engineering and Materials Science, University of California, Irvine, California 92697-2575, USA*

[4]*Laser Microbeam and Medical Program, Beckman Laser Institute, University of California, Irvine, California 92612-3010, USA*

(Received 7 June 2011; published 25 January 2012)

Laser-induced breakdown of an optically trapped nanoparticle is a unique system for studying cavitation dynamics. It offers additional degrees of freedom, namely the nanoparticle material, its size, and the relative position between the laser focus and the center of the optically trapped nanoparticle. We quantify the spatial and temporal dynamics of the cavitation and secondary bubbles created in this system and use hydrodynamic modeling to quantify the observed dynamic shear stress of the expanding bubble. In the final stage of bubble collapse, we visualize the formation of multiple submicrometer secondary bubbles around the toroidal bubble on the substrate. We show that the pattern of the secondary bubbles typically has its circular symmetry broken along an axis whose unique angle rotates over time. This is a result of vorticity along the jet towards the boundary upon bubble collapse near solid boundaries.

DOI: 10.1103/PhysRevE.85.016319 PACS number(s): 47.55.D−, 87.80.Cc, 42.62.Be, 87.50.wf

I. INTRODUCTION

Cavitation dynamics have been at the heart of a range of key physical developments in the last century. Such cavitation has important consequences for a range of studies including those in fluid mechanics, shock wave dynamics, biophysical processes, and even carbon nanotube manipulation [1–5]. In this domain, laser-induced breakdown (LIB) is an established powerful method where the large electric field strength of a high-intensity laser pulse initiates breakdown within a medium [6,7]. The energy deposition during optical breakdown causes a rapid temperature and pressure increase within the plasma, thereby initiating its explosive expansion. When formed in a liquid, the breakdown is followed by the formation of a shock wave and the expansion of a cavitation bubble. The recent use of optical breakdown of a trapped nanoparticle within a liquid environment [8] opens up new vistas in this field by providing a powerful test system for exploring hitherto unanswered physical questions regarding cavitation dynamics, bubble formation, and evolution. Such dynamical processes are central to a range of key techniques, particularly in the biomedical sciences including targeted cell lysis and dissection or inactivation of material such as cellular organelles, cytoskeletal filaments, and chromosomes [9–11]. Such breakdown is also essential to the targeted delivery of genes or biomolecules via transient permeabilization of the plasma membrane of a cell (photoporation) [8,12]. In the domain of plasma membrane permeabilization, the cellular response to cavitation-induced shear stress resulting from the LIB of an optically trapped nanoparticle was studied using time-resolved quantitative phase microscopy [13].

In this paper we investigate the LIB of an optically trapped nanoparticle in aqueous media near a rigid boundary using a nanosecond laser pulse. This system enables us to study the dynamics of cavitation and secondary bubbles in a low-energy regime (typically two orders of magnitude lower than breakdown in water alone) as the threshold energy required for LIB is dependent on the nanoparticle material and its size and is independent of the surrounding medium [8]. We visualize the intricate symmetry of the secondary bubbles resulting from the cavitation bubble collapse along with the jet flow towards the boundary. Further, we find that the pattern of the secondary bubbles has its circular symmetry broken along an axis whose unique angle rotates with time. This reflects vorticity involved with the jet towards the boundary upon bubble collapse near solid boundaries.

We employ nanosecond time-resolved imaging to quantify the spatial and temporal dynamics of the cavitation and secondary bubbles evolution. A temporal resolution of ∼1 ns is achieved by the use of a nanosecond laser as the illumination source. We investigate more than 5000 events at times between 50 ns and 260 μs after the LIB of a single nanoparticle. The dynamic shear stress from the expanding bubble is quantified using a hydrodynamic model based on the spatial and temporal evolution of both the radial position and velocity of the bubble wall [14]. In the presence of a cell monolayer, we verify the maximum shear stress at radial positions corresponding to the regions of necrotic and permeabilized cells by the molecular injection experiment. Additionally our results confirm that LIB of nanoparticles with nanosecond laser sources offers unprecedented confinement of cavitation bubbles compared to that from nanosecond LIB of a liquid alone [8].

II. EXPERIMENTAL SETUP

In the experiment, a 1070-nm continuous wave (CW) fiber laser (IPG Laser GmbH, YLM-5-1070-LP: power ∼80 mW) was focused by a microscope objective (Nikon

*Author to whom correspondence should be addressed to: ya10@st-andrews.ac.uk or ma81@st-andrews.ac.uk

Ltd., E plan 100 × 1.25NA, oil immersion) to optically trap a polystyrene nanoparticle (400 nm in diameter) in water. The nanoparticle was held at a predefined location of either 10 μm or 16.5 μm above the substrate. A single pulse from a 532-nm frequency doubled Q-switched Nd:YAG laser (Elforlight Ltd., SPOT: pulse width ~1 ns, energy ~1 μJ) was coaligned with the trapping beam and focused through the same objective onto the trapped nanoparticle. Time-resolved imaging was achieved by using a second 532-nm Nd:YAG laser (Elforlight Ltd., SPOT: pulse width ~1 ns, energy $\leqslant$1 μJ), which delivered a single pulse at a desired time delay after the LIB event. A delay pulse generator (Directed Energy, Inc., PDG-2515) was used to trigger both the nanosecond lasers (one for LIB and the other for illumination) with a desired timing. Images of the LIB events, at time delays between 50 ns and 260 μs, were recorded by a CCD camera (Imaging Source, DMK31BU03) triggered synchronously with the nanosecond lasers. As a result, one stroboscopic image was captured for each triggered LIB event (Supplemental Material [15]).

III. HYDRODYNAMIC ANALYSIS OF THE DYNAMICS OF PRIMARY MICROBUBBLES

Figure 1(a) shows a series of time-resolved images of expansion and collapse of the cavitation bubble initiated at an axial position, Z_0 of 16.5 μm from the substrate (Supplemental Material [15]). The maximum bubble radius, $R_{\max}$, reached ~35 μm at ~3 μs, which is typically an order of magnitude smaller than that of the LIB of a liquid [14,16]. Due to the close proximity of the bubble to the substrate with a stand-off parameter $\gamma \sim 0.47$ ($=Z_0/R_{\max}$), a jet flow directed towards the substrate at the center of the bubble was formed in the collapse phase of ~7–8 μs. Time-resolved imaging provides a means to quantify the spatial and temporal evolution of both the radial position $R_B(t)$ [Fig. 1(b)] and velocity $V_B(t)$ [Fig. 1(c)] of the bubble wall. A minimum of ten images was used to obtain the average and standard deviation (2σ) at each data point shown for the axial locations of $h = 10$ and 16.5 μm. Here we follow the hydrodynamic analysis proposed by Rau *et al.* [14] to obtain the transient shear stress at various radial positions. Firstly, the transient external fluid velocity $V_\infty(r,t)$ produced by the cavitation bubble expansion was determined by applying the conservation of mass for an incompressible fluid in spherical coordinates:

$$V_\infty(r,t) = V_B(t)\left[\frac{R_B(t)}{r}\right]^2. \tag{1}$$

Secondly, conservation of momentum was applied to obtain the transient wall shear stress $\tau_w(r,t)$ generated by the cavitation bubble expansion:

$$\tau_w(r,t) = \rho\sqrt{\frac{\nu}{\pi}}\int_0^t \frac{\partial V_\infty(r,t')}{\partial t'}\frac{dt'}{\sqrt{t-t'}}, \tag{2}$$

where ρ ($=1000$ kg m^{-3}) and ν ($=0.896\times10^{-6}$ m^2 s^{-1}) are the density of the liquid and kinematic viscosity of the buffer medium. Equation (2) is valid at any radial position r and time $0 < t < t'$ where t' is the time of arrival of the bubble wall at position r. The temporal profile of the wall shear stress at different radial positions is shown in Fig. 1(d). As expected, the maximum shear stress decreases with increasing radial position [Fig. 1(e)]. It should be noted that the model assumes that the bubble center is located at the surface of the substrate, i.e., for γ approaching zero so that the plasma location does not break the spherical symmetry of the system. The use of this model to predict shear stresses for $\gamma = 0.3-0.5$ would slightly overestimate the true shear stress since the velocity gradients at the boundary will be lower. It is worth mentioning that due to the smaller bubble sizes, the maximum wall shear stress produced by the LIB of a nanoparticle at equivalent

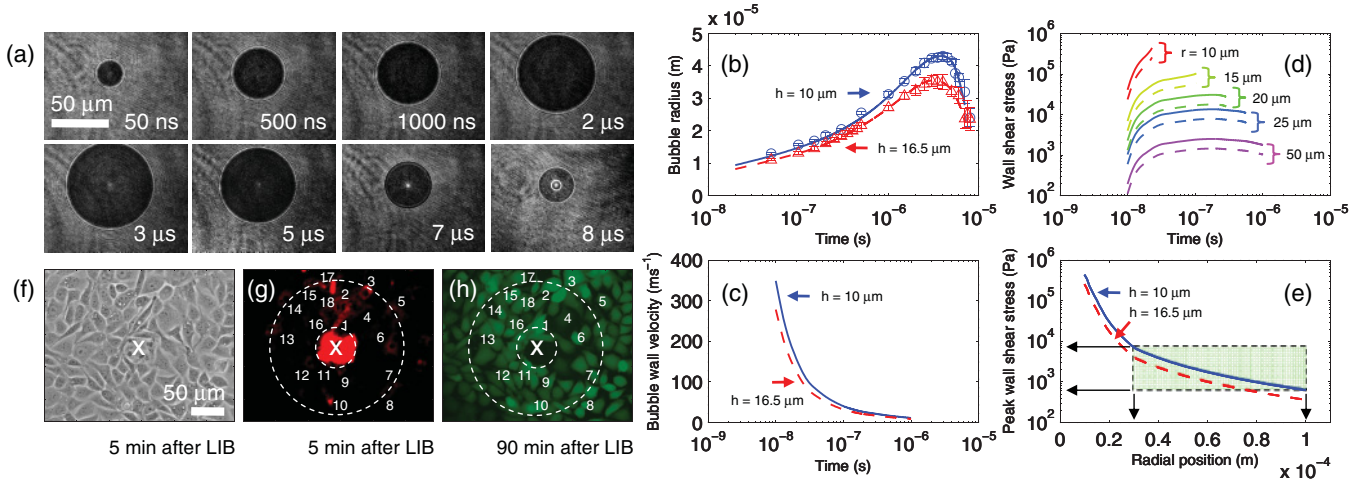

FIG. 1. (Color online) Dynamics of cavitation and shear stress at radial positions from expanding bubble wall and delivery of molecules (PI) into multiples of CHO-K1 cells with CAM viability assay. (a) Time-resolved images of cavitation bubble. (b) Cavitation bubble dynamics. (c) Bubble wall velocities. (d) Temporal shear stress at radial positions. Solid and broken lines represent $h = 10$ μm and 16.5 μm, respectively. (e) Maximum shear stress at radial positions. (f) Phase contrast image of cells where "×" denotes the site of LIB. (g) Fluorescence image of cells showing uptake of PI. (h) Fluorescence image of cells showing their cell viability using CAM.

radial locations is typically two orders of magnitude lower than those in previous studies where the LIB was performed in aqueous media alone [14].

IV. DELIVERY OF MOLECULES INTO LIVING CELLS

We recently demonstrated plasmid-DNA transfection of cells with the LIB of a nanoparticle [8]. We found that the efficiency of transfection can be optimized by the LIB parameters such as the nanoparticle size and its location relative to the cell monolayer at which LIB is performed. It is of particular interest to quantify the maximum shear stress at radial positions corresponding to the region of cells permeabilized. To verify this, delivery of molecules of propidium iodide (PI) into CHO-K1 cells was examined with the LIB of a single polystyrene nanoparticle (400 nm in diameter) positioned at 10 μm from the cell monolayer (Supplemental Material [15]). PI is a membrane impermeable substance and becomes fluorescent once it binds to nucleic acids within the cell. Cell viability was assayed using Calcein-AM (CAM) whose fluorescence intensity associates with two cell viability indicators—concentration of esterases and integrity of the plasma membrane [17]. Figures 1(f)–1(h) show typical phase contrast and fluorescence images of cells exposed to PI and CAM. It shows that four cells right next to the LIB ($0 \leqslant r < 30$ μm) are necrotic whereas 18 cells [numbered in Figs. 1(g) and 1(h)] in the region of $30 \leqslant r < 100$ μm (an enclosed area between two circles) exhibit uptake of PI with retention of cell viability, 90 min after the LIB. By comparing these with Fig. 1(e), the maximum wall shear stress $\tau_{w,max} \geqslant$ 10 kPa at a radial position between 0 and 30 μm leads to cell necrosis, while $\tau_{w,max} \sim$ 1–10 kPa in the range of $30 \leqslant r < 100$ μm can enhance the membrane permeability of CHO-K1 cells without any loss in cell viability. These values of shear stress are in good agreement with the results of the previous studies on cell permeabilization resulting from the LIB of a liquid [12]. Importantly, no lysis zone of cells is observed by the LIB of a nanoparticle. Thus, this approach has a clear advantage in cavitation control, which can be optimized for delivery of molecules or transfection of cells in a targeted area, while reducing cell lysis. It should be noted that jetting followed by the radial flow on the substrate induces shear stresses. A hydrodynamic model formulated by Glauert can be used to estimate the shear stress formed by the jet [18]. Ohl *et al.* modeled the shear stress for the bubble radius of $R_{max} = 50$ μm and showed that the maximum shear stress by the jet at $r =$ 20 μm does not exceed 1 kPa [19], which is approximately two orders of magnitude lower than the shear stress caused by the bubble wall expansion. Thus, the shear stresses associated with cavitation bubble expansion is the primary cause of cellular membrane permeabilization.

V. AXIAL SYMMETRY AND ROTATION OF SECONDARY MICROBUBBLES

One of the most important features of cavitation is its interaction with nearby boundaries. A cavitation bubble close to a rigid boundary with a stand-off parameter $\gamma \approx 0.47$ tends to collapse asymmetrically, often forming high-speed liquid jets directed towards the wall [Fig. 1(a), ~8 μs]. As the jet traverses the cavitation volume, the toroidal bubble is formed along the jet axis and is subdivided into multiple bubbles [Figs. 2(a)–2(c)]. The subsequent radial flow along the substrate plane can be accompanied by submicrometer secondary bubbles at the leading edge of the radial flow around the toroidal bubbles [Figs. 2(a)–2(c)]. Thus we have a direct observation of both the formation of secondary bubbles and division of a toroidal ring bubble. These observations confirm the conclusions of the cavitation erosion mechanism proposed in previous work [20,21].

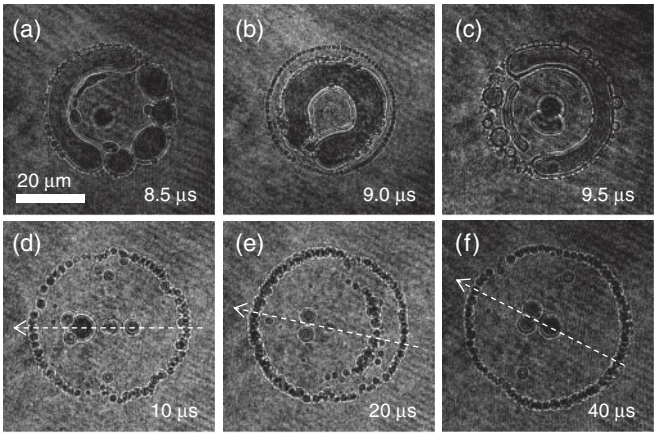

FIG. 2. Formation of toroidal ring bubbles and secondary bubbles. (a)–(c) Division of toroidal ring bubble and formation of submicrometer secondary bubbles. (d)–(f) Axial symmetry of the formed patterns of secondary bubbles and their rotation over time.

Figures 2(d)–2(f) show a striking axial symmetry of the formed patterns of secondary bubbles between 10 and 40 μs. For the image analysis, the secondary bubbles were treated as binary objects, where the axis was defined as a line passing through the center of mass of bubble objects with the lowest total moment of inertia. The distribution of orientation angles associated with the axis at different times is shown in Fig. 3(a). The normal distribution curve was fitted to experimental data,

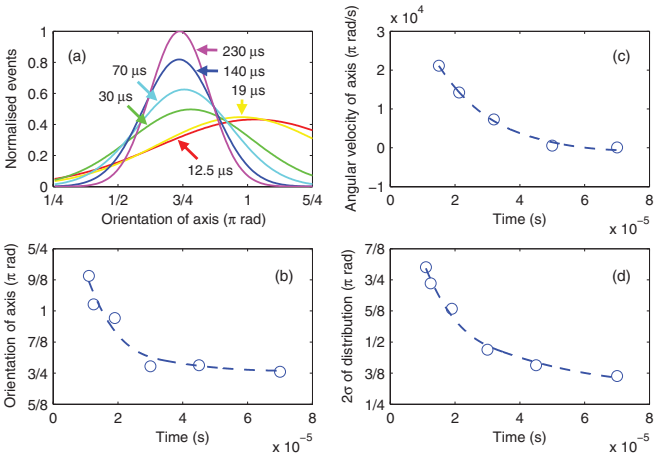

FIG. 3. (Color online) Analysis of axial symmetry of the formed patterns of secondary bubbles. (a) Angular distribution of axes of symmetry at times. (b) Mean angle of axes over time. (c) Angular velocity of axes over time. (d) Standard deviation (2σ) of angular distribution of axes over time.

where the total area under the curve over $\pi/4$–$5\pi/4$ rad was normalized to unity. Noticeably, the axis of symmetry rotates clockwise from $\sim\pi$ rad at $t \approx 10$ μs towards $\sim 3\pi/4$ rad at $t \approx 50$ μs [Figs. 3(a) and 3(b)]. It is also worth noting that the standard deviation of the distribution becomes narrower over time [Figs. 3(a) and 3(d)]. The angular velocity of the axis was found to be $\sim 2\times 10^4 \pi$ rad s^{-1} at $t \approx 10$ μs and decays rapidly to zero at $t \approx 50$ μs [Fig. 3(c)].

The axial breakage of circular symmetry reflects the dynamics of energy transfer in the LIB system. In cases where spherical symmetry is maintained during the entire process of LIB including plasma formation followed by cavitation, the subsequent bubble collapse towards the boundary will result in a circularly symmetric pattern of secondary bubbles. It was previously shown in the LIB of a liquid that a small asymmetry in the plasma formation induced by the so-called "moving breakdown" transfers to the subsequent processes during the collapse phase [22]. This can break the circular symmetry in the formation of toroidal bubbles, which leads to an asymmetric pattern of surface erosion [21]. In our case, the LIB of a nanoparticle has a unique axis in the system, defined by the positions of the nanosecond laser focus and the center of the optically trapped nanoparticle. The discrepancy in the lateral positions between these two points results in asymmetric plasma formation, which in turn breaks the circular symmetry of the formed pattern of secondary bubbles.

The rotation of the axis of symmetry over time indicates further breakage of the axial symmetry. It was previously suggested that the jet flow involves vorticity around its axis in the LIB of a liquid [23], which can lead to the breakage of the circular symmetry. Here, the authors attributed the vorticity to instabilities, which were probably caused by a slight asymmetric impingement of the reentrant liquid jet onto the opposite bubble wall. However, the reproducibility of this process was unclear. In our LIB system, both the direction and magnitude of the vorticity are statistically consistent in a large data set, which suggests an external, nonspontaneous mechanism of symmetry breakage. This systematic breakage of circular symmetry can be induced by a characteristic geometry of the system. In our case, we believe asymmetric breakdown, due to the discrepancy in the positions between the nanosecond laser focus and the center of the optically trapped nanoparticle, results in the rotation of the axis of symmetry in the pattern of secondary bubbles. It is worth noting that the shear flow created by the vorticity around the vertical axis is two orders of magnitude lower compared to the radial flow caused by the expanding bubble. The broader distribution of the orientation angle of the axis at times immediately after the cavitation collapse ($10 < t < 20$ μs) is mainly a result of the remaining toroidal ring bubbles.

VI. STAND-OFF PARAMETER, γ DEPENDENCE OF SECONDARY MICROBUBBLES

Another important aspect of bubble collapse near solid boundaries is cavitation erosion on the substrate. In this respect, we further investigated the formation of secondary bubbles with different stand-off parameters, γ from 0.23 to 0.51. Figures 4(a)–4(g) show typical secondary bubbles formed on the substrate at 50 μs after LIB. We note that the uniformity and

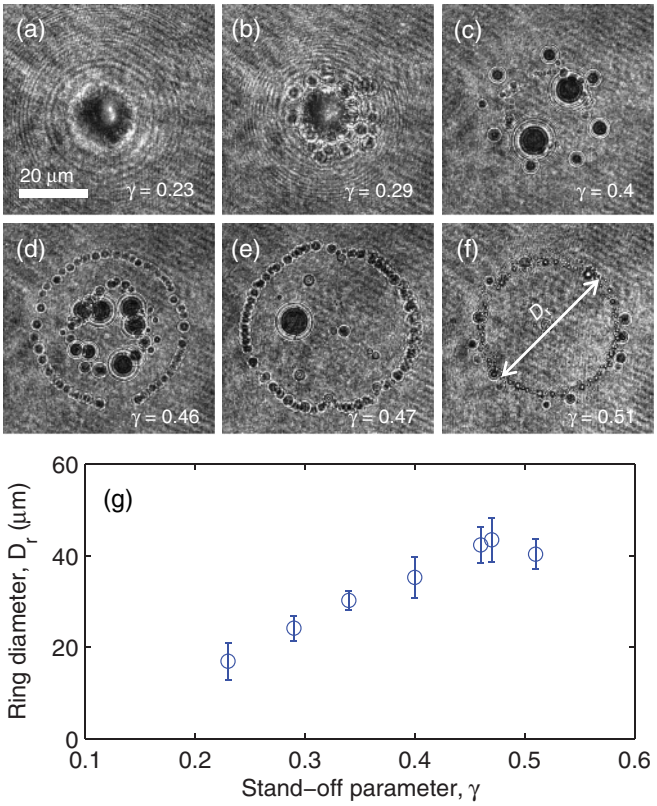

FIG. 4. (Color online) Formation of secondary bubbles with different stand-off parameters, γ from 0.23 to 0.51. (a)–(f) Bright field images of secondary bubbles formed on the substrate at 50 μs after LIB. (g) Correlation between γ and average ring diameter, D_r of secondary bubbles.

dimensions of the formed pattern of secondary bubbles are reasonably consistent over 10–50 μs for a constant γ [Figs. 2(d)–2(f)]. However, they are strongly dependent on γ, in which the average ring diameter of the formed secondary bubbles, D_r increases as γ increases (Fig. 4). A similar pattern was observed in the circular pit (damaged patterns on indium specimens) formation in previous work [20,21]. This supports their conclusions of the cavitation erosion mechanism, which is attributed mainly to the collapse of toroidal and/or secondary bubbles.

VII. CONCLUSIONS

In this paper, the spatial and temporal dynamics of the cavitation and secondary bubbles resulting from the LIB of an optically trapped single nanoparticle were quantified using nanosecond time-resolved imaging. Hydrodynamic modeling was used to determine the dynamic shear stress produced by the expanding bubble. The maximum shear stress at radial positions corresponding to the region of the cells permeabilized was verified by the delivery of PI molecules into a CHO-K1 cell monolayer. The technique was shown to minimize the energy required for controllable cavitation, which leads to the permeabilization of cells in a targeted area with good retention of cell viability. The final stage of cavitation collapse was investigated using a large data set. We visualized the formation of secondary bubbles around the subdividing toroidal ring bubble. We also determined the axis

of symmetry in the formation of secondary bubbles and its rotation upon bubble collapse near solid boundaries.

In conclusion, LIB of an optically trapped nanoparticle offers a method to control cavitation size down to tens of micrometers and to systematically induce vorticity around the jet towards the boundary. The technique has the potential to increase the applicability and understanding of a number of physical processes including cell transfection, fluid dynamics, shock wave processes, sonoluminescence, and blood flow dynamics.

ACKNOWLEDGMENTS

We thank the UK Engineering and Physical Sciences Research Council (EPSRC) and Scottish Universities Life Sciences Alliance (SULSA) for funding. V.V. acknowledges support from the Laser Microbeam and Medical Program, Grant No. NIH-P41-RR01192. M.A. acknowledges support from an EPSRC funded University of St Andrews Rising Star Fellowship. K.D. acknowledges support from a Royal Society Wolfson-Merit Award.

[1] V. Venugopalan, A. Guerra, K. Nahen, and A. Vogel, Phys. Rev. Lett. **88**, 078103 (2002).
[2] M. S. Hutson and X. Y. Ma, Phys. Rev. Lett. **99**, 158104 (2007).
[3] E. Zwaan, S. Le Gac, K. Tsuji, and C. D. Ohl, Phys. Rev. Lett. **98**, 254501 (2007).
[4] P. A. Quinto-Su, X. H. Huang, S. R. Gonzalez-Avila, T. Wu, and C. D. Ohl, Phys. Rev. Lett. **104**, 014501 (2010).
[5] T. Pezeril, G. Saini, D. Veysset, S. Kooi, P. Fidkowski, R. Radovitzky, and K. A. Nelson, Phys. Rev. Lett. **106**, 214503 (2011).
[6] C. E. Bell and J. A. Landt, Appl. Phys. Lett. **10**, 46 (1967).
[7] P. A. Barnes and K. E. Rieckhof, Appl. Phys. Lett. **13**, 282 (1968).
[8] Y. Arita, M. L. Torres-Mapa, W. M. Lee, T. Čižmár, P. Campbell, F. J. Gunn-Moore, and K. Dholakia, Appl. Phys. Lett. **98**, 093702 (2011).
[9] E. L. Botvinick, V. Venugopalan, J. V. Shah, L. H. Liaw, and M. W. Berns, Biophys. J. **87**, 4203 (2004).
[10] A. Vogel, K. Lorenz, V. Horneffer, G. Huttmann, D. von Smolinski, and A. Geberty, Biophys. J. **93**, 4481 (2007).
[11] P. A. Quinto-Su, H. H. Lai, H. H. Yoon, C. E. Sims, N. L. Allbritton, and V. Venugopalan, Lab Chip **8**, 408 (2008).
[12] A. N. Hellman, K. R. Rau, H. H. Yoon, and V. Venugopalan, J. Biophotonics **1**, 24 (2008).
[13] M. Antkowiak, Y. Arita, K. Dholakia, and F. J. Gunn-Moore, J. Biomed. Opt. **16**, 120508 (2011).
[14] K. R. Rau, P. A. Quinto-Su, A. N. Hellman, and V. Venugopalan, Biophys. J. **91**, 317 (2006).
[15] See Supplemental Material at http://link.aps.org/supplemental/10.1103/PhysRevE.85.016319 for experimental methods and figure of experimental setup.
[16] K. R. Rau, A. Guerra, A. Vogel, and V. Venugopalan, Appl. Phys. Lett. **84**, 2940 (2004).
[17] C. M. Pitsillides, E. K. Joe, X. B. Wei, R. R. Anderson, and C. P. Lin, Biophys. J. **84**, 4023 (2003).
[18] M. B. Glauert, J. Fluid Mech. **1**, 625 (1956).
[19] C. D. Ohl, M. Arora, R. Ikink, N. de Jong, M. Versluis, M. Delius, and D. Lohse, Biophys. J. **91**, 4285 (2006).
[20] Y. Tomita and A. Shima, J. Fluid Mech. **169**, 535 (1986).
[21] A. Philipp and W. Lauterborn, J. Fluid Mech. **361**, 75 (1998).
[22] P. K. Kennedy, D. X. Hammer, and B. A. Rockwell, Prog. Quantum Electron. **21**, 155 (1997).
[23] E. A. Brujan, G. S. Keen, A. Vogel, and J. R. Blake, Phys. Fluids **14**, 85 (2002).